Crack-Parallel Tension Effects on Fracture of Soft Knitted Polymer Composites deduced from Gap Tests via Microplane Triads

Xiaoxiao Ding,[1] Yanzhao Niu,[2] Yang Zhao,[2] Hongshun Chen,[1] Chanhyeong Bae,[3] Anh Tay Nguyen,[2] Horacio D. Espinosa,[1] Zdeněk P Bažant,[1, 2, 3, *] and Jian Cao[1, 2, 3, †]

[1]*Department of Mechanical Engineering, Northwestern University, USA*
[2]*Department of Civil and Environmental Engineering, Northwestern University, USA*
[3]*Department of Materials Science and Engineering, Northwestern University, USA*

(Dated: June 12, 2026)

Soft composites are increasingly used in wearable and soft robotic systems as advances in material architecture enable greater damage tolerance under large deformation. In these mesoscale architectures, the crack-parallel stresses bias geometric rearrangements of reinforcement fibers, modifying the crack initiation and growth beyond the opening-mode fracture. Here, we introduce a tensile gap test to quantify how the crack-parallel stress affects the onset and trajectory of damage localization, as well as the load- and energy-based fracture responses. We also develop and experimentally validate a continuum model that captures nonlinear behavior and progressive damage of knitted composites, using an ensemble of oriented microplane triads aligned with the yarn direction, capturing the axial load-transfer mechanisms while incorporating the transverse and shear effects. Together, the experiments and the computational model provide a tool to predict fracture under realistic stress states and to guide the rational design of soft composites in engineering applications.

Knitted fabric embedded in a soft polymer matrix, such as PDMS (polydimethylsiloxane) or PDMA (polydimethylacrylamide-based hydrogel), i.e., soft knitted polymer composites, have a great potential for soft robots [1–3], wearable sensors [4–7], and engineered tissues [8–10]. Their usefulness, however, is limited by fracture. Yet predicting their fracture faces three challenges: (1) formulating a realistic continuum model for the knitted composites at large strain, (2) clarifying experimentally the effect of crack-parallel stress on the material fracture energy, and (3) replacing the LEFM (linear elastic fracture mechanics) by a fracture model that takes into account the expected dependence of the material fracture energy on the nonsingular crack-parallel stress components. To obtain a continuum model for knitted composites, we adopt the microplane triad model [11, 12], originally formulated for woven composites with much smaller yarn undulation. Here, we introduce testing of center-notched fracture specimens under various levels of constant crack-parallel tension (illustrated in Fig. 1). The results show that this tension causes a large increase in the fracture energy (a measured effective value, G_f) of the soft knitted polymer composites.

This new phenomenon implies a finite-width anisotropic damage zone at the crack front, which can be captured in finite element analysis (FEA) via a crack-band formulation on an appropriate representative volume element (RVE) or, more accurately, via a second-gradient regularization based on the new spress-sprain concept [13, 14]. The variability of G_f has previously been demonstrated in a range of material systems, including concrete [15–17], woven composites [18], soft rubber [19], and perfect cracks in atomic lattices [20]. These observations suggest that variability in material fracture energy may reflect a ubiquitous and fundamental fracture mechanism, motivating the present examination of fracture mechanics in soft knitted polymer composites.

For soft knitted polymer composites, competition between the energy dissipation at the yarn-level and at the damage-zone-scale controls how the fracture proceeds through stages of distributed damage. It is analogous to the competing length-scale mechanisms in soft tough materials [21–23], but is additionally shaped by the geometrically biased yarn rearrangements within the knitted architecture [24].

Modeling the fracture of soft knitted polymer composites is challenging. One aspect is the development of a continuum model that accounts for nonlinearity arising from large strains in these composites, from the softness of the knitted architecture [25, 26] and the polymer matrix, PDMS [27, 28]. Analogous to human tissues [29, 30], very large strains lead to nonlinear stiffening and an elevated damage tolerance due to progressive yarn reorientation with load transfer to the neighboring yarns.

On the other hand, discrete-yarn models [25, 31, 32] can capture yarn-level kinematics, but inferring the material fracture behavior is computationally expensive. In contrast, continuum damage models are relatively efficient [33–36], but struggle to capture the directional yarn behavior that controls crack growth.

An effective approach is offered by the microplane triad model, earlier introduced to represent the mild undulation of the yarn in a woven twill [11, 12]. To adapt this model for knits, a triad of mutually orthogonal microplanes is attached at each of several chosen characteristic points within the RVE (shown in Fig. 2C).

In each loading step of an explicit finite element computation, the continuum strain tensor obtained at the end of the previous loading step is related to the strain tensor on each microplane. A simple tensorial constitutive

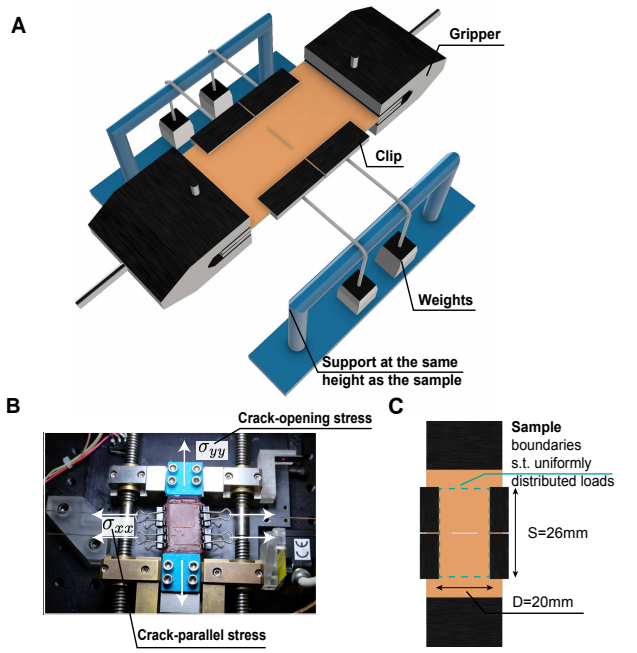

FIG. 1. Experimental design and setup of the tensile gap test. (A) 3D model of the setup showing customized components used to transfer and secure the applied loads. (B) Close-up view of the tester showing how crack-opening tension and crack-parallel stress are applied. (C) Simplified 2D view of the setup showing sample boundaries subjected to uniformly distributed loads from the grippers and clips, with sample dimensions indicated.

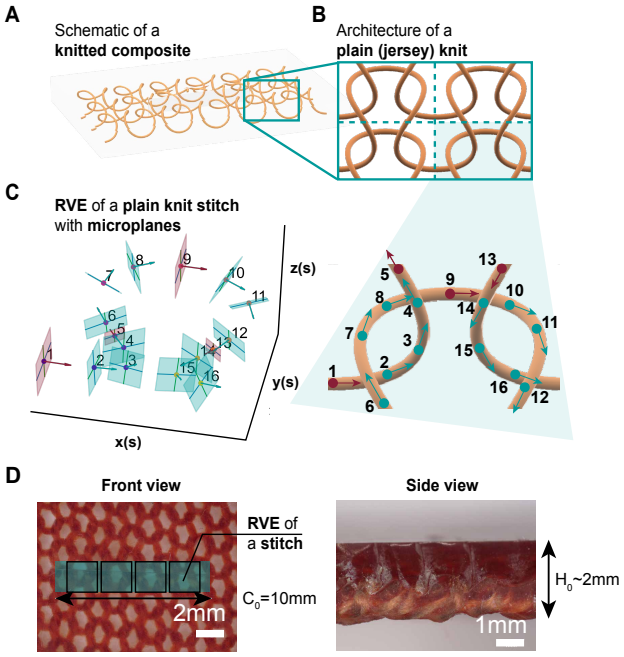

FIG. 2. Setup of the microplane-triad model for a representative volume element (RVE) of a plain (jersey) knit stitch. (A) Schematic of a knitted composite (the number of stitches shown within the region of interest is reduced for clarity). (B) Architecture of a plain knit [25]. (C) RVE of a plain knit stitch, with microplane triads shown in 3D parametric space (left) and in a 2D projection (right). Note that only a single stitch, rather than the 2 by 2 stitches often used for defining a RVE of a general knitted fabric architecture, is selected because of the periodicity of the plain (jersey) knitted architecture. (D) Microscopy images of the front and side views of a knitted soft composite specimen, with the initial notch length equivalent to four RVE widths and the specimen thickness indicated.

law on the microplane level is then used to calculate new microplane stress tensors. The variational principle of virtual work then yields the new continuum (macro-scale) stress tensor at the end of the current loading step [37].

To clarify the role of the crack-parallel tension, we take advantage of its expected relatively small magnitudes, compared to concrete or stiff and non-stretchy composites. Hence, a constant crack-parallel stress can be generated by manageable weights, as illustrated by the first tensile gap test in Fig. 1, in which center-notched specimens are transversely loaded through weights suspended on nylon strings sliding with negligible friction over horizontal support bars, while the crack opening force is applied under displacement control in the longitudinal y direction.

Overall, we combine fracture experiments with microplane triad-based elastic and damage models to determine how crack-parallel stress controls fracture in soft knitted polymer composites. First, we systematically vary the crack-parallel stress while maintaining controlled crack-opening conditions. Second, we document damage stages in soft knitted polymer composites, including microcracking in the soft polymer matrix, yarn tautening, yarn sliding, yarn rupture and post-peak softening. Third, we computationally implement the calibrated microplane triad model and use it to verify the experimentally observed sensitivity of material fracture energy to the crack-parallel stress. By coupling the experiment and the microplane triad model, we link the yarn-scale damage evolution in the knitted architecture to the macroscopic fracture initiation and propagation under realistic complex loading conditions.

RESULTS

Tensile gap tests reveal sensitivity to crack-parallel stress

Fig. 3A shows the force–displacement curves measured under three crack-parallel stress levels, $\sigma_{xx} = 0$, 384 kPa, and 872 kPa, with crack-opening tension applied under displacement control to induce mode-I fracture. These crack-parallel stress levels were selected to span the experimentally accessible range: $\sigma_{xx} = 0$ provides the reference condition, $\sigma_{xx} = 872$ kPa approaches the maximum stress permitted by the bonding strength between the clips and the specimen, and $\sigma_{xx} = 384$ kPa represents an intermedi-

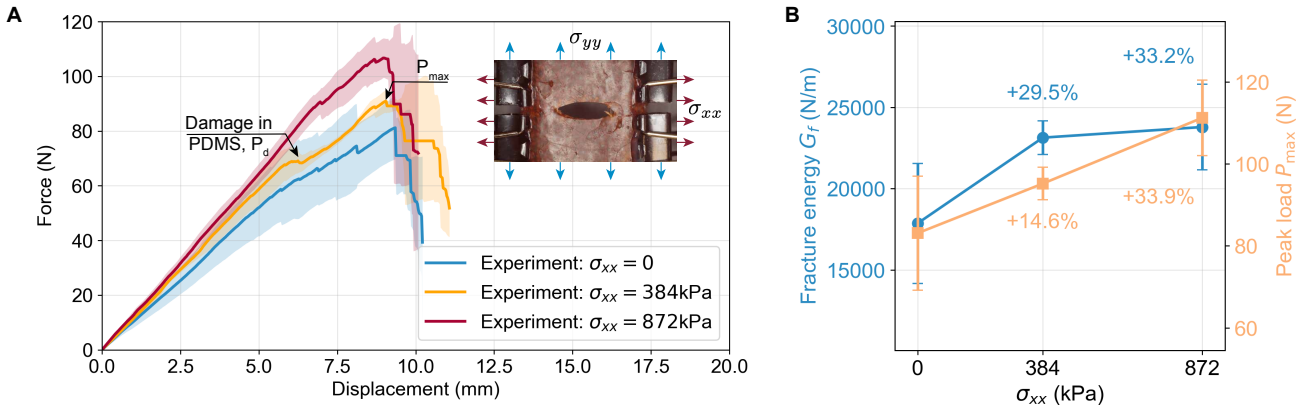

FIG. 3. Fracture experiments measuring responses to various crack-parallel stresses: (A) Force–displacement curves plotted as the mean of at least three tests; the shaded region represents ± one standard deviation. (B) Fracture energy G_f and peak load P_{max} as a function of the crack-parallel stress σ_{xx}.

ate loading condition. The observed first drop in load P_d indicates damage occuring the soft polymer matrix prior to reaching the ultimate peak load P_{max}. Assuming that no energy is dissipated away from the fracture process zone, the fracture energy, G_f, is calculated as $G_f = W/A$ where W is the work of fracture calculated from the area under the force-displacement curve (under the assumption of no dissipation elsewhere),

$$W = \int F \, d\delta, \tag{1}$$

Here F is the measured force and δ is the imposed displacement, normalized by an effective crack surface area as $A = C_0 H_0$ in which C_0 is the initial crack length and H_0 is the specimen thickness measured from microscopic images shown in Fig. 2D.

The overall response shows (i) an initial quasi-linear regime, (ii) a staged-approach to peak load P_{max} associated with crack blunting and bridging engagement with the PDMS getting damaged at load P_d, and (iii) a post-peak regime characterized by steep stepwise load drops. The post-peak features indicate progressive rather than catastrophic loss of load-carrying capacity, consistent with sequential engagement and rupture of bridging yarns.

Under constant crack-parallel tensile stress, the force-displacement response exhibits monotonically increasing peak load P_{max} and elevated fracture energy G_f, relative to the no crack-parallel-stress, $\sigma_{xx} = 0$. Note in Fig. 3B the remarkable increase of G_f.

The effect of the crack-parallel stresses revealed by the tensile gap tests shows that a *damage zone of finite width* must exist at the fracture front. For accurate computations, this is a major complication requiring incremental finite strain analysis. In addition, for widely opened blunted cracks at large strain, there exists no simple analytical size effect law, such as that for quasi-brittle stiff materials.

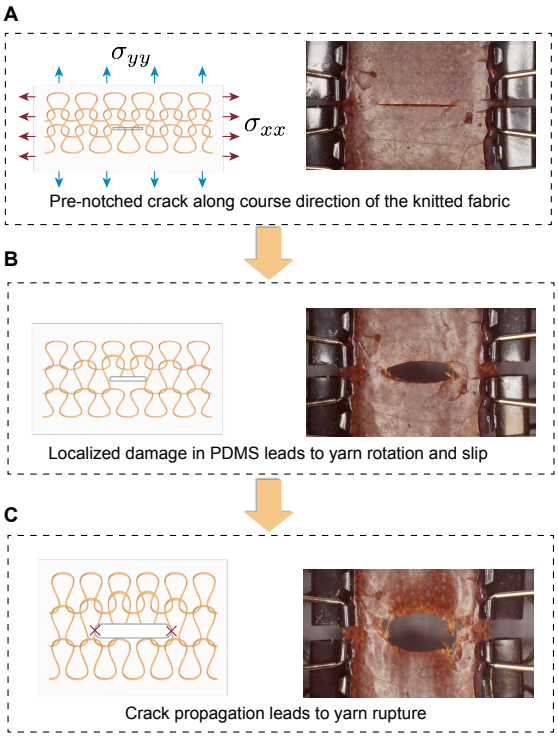

FIG. 4. Schematics and in-situ images from tensile gap tests showing links across microscale deformations, mesoscale process zone and macroscopic response.

In-situ imaging shows a gradual multi-scale damage development

To relate the macroscopic force–displacement response to underlying mechanisms, we analyzed in-situ camera images of the specimen and illustrated the main mechanisms as schematics in Fig. 4. Prior to visible matrix damage (Fig. 4A), the notch tip remains relatively sharp and the

deformation is accommodated primarily by modest localized yarn deformation. Once PDMS damage initiates (Fig. 4B), as evidenced by localized microcrack formation near the notch tip, the crack tip undergoes pronounced blunting: the tip radius increases, the opening localizes into a finite-width damage zone rather than a sharp advancing crack. This mesoscale damage zone provides an environment that facilitates localized yarn rotation and sliding in the vicinity of the crack tip, delaying localization into immediate yarn rupture. As loading proceeds beyond the onset of blunting, yarns spanning the crack wake progressively straighten and become taut, concentrating load into a subset of bridging segments. The onset of yarn rupture (Fig. 4C) marks the transition to post-peak softening as bridging tractions get progressively lost. Under crack-parallel tensile stress, this sequence is biased toward stronger engagement of bridging during the blunted-tip phase, which sustains higher forces over a broader displacement range and increases the macroscopic work of fracture that infers the fracture energy.

Model validation: Simulations reproduce damage localization and crack evolution

Simulations using the microplane triad damage model reproduce: (i) the dependence of peak load on crack-parallel stress level, (ii) the onset and trajectory of localization bands, and (iii) the transition from distributed matrix damage to localized bridging loss. Fig. 5 compares the predicted and experimentally observed responses, which shows overall agreement. Enabled by simulations, we can probe into the internal stress fields at varying stages of damage evolution, which is otherwise difficult to obtain directly from experiments. Fig. 6 shows the stress component σ_{xx}, whereas Fig. 7 shows the stress component σ_{yy} at two critical stages: (A) damage in the PDMS matrix and (B) damage in the yarns.

DISCUSSION

Stress-state dependent fracture energy: why G_f is not a material constant in knitted composites

A central implication of the tensile gap tests is that the fracture energy G_f inferred from macroscopic work of fracture increases with the crack-parallel stress. Like in other matierals, in knitted composites, the damage zone must be a region of finite width where matrix microcracking, yarn rotation, sliding, bridging, tautening and rupture take place and interact. The crack-parallel tensile stress alters the sequence and spatial distribution of these mechanisms, changing the peak response and the post-peak evolution and thereby the work dissipated during fracture. Consequently, design with G_f as a unique material constant, independent of crack-parallel stress, is incorrect and misleading.

The gap test concept for soft composites

The gap test in quasibrittle fracture of hard heterogenous materials means, in general, that nonsingular compressive crack-parallel stresses can change the damage in the fracture process zone (FPZ) and cause the material fracture energy to increase or decrease. Our tensile results provide a demonstration for soft textile composites, in which the damage is governed by textile mesostructure and geometric nonlinearity at large strain. Unlike concrete and rock, the knitted composites exhibit a discrete-yarn network whose capacity of bridging soft zones of matrix gets exhausted and whose rupture can occur in a stepwise manner. These observations may explain why the crack-parallel stress can change the total work of fracture noticeably while producing a comparatively smaller net change in the peak load.

Implications for design and for predictive modeling

For wearable and soft robotic systems, crack-parallel stresses are ubiquitous due to seams, attachments, bending, and contact. The present results indicate that durability cannot be appraised using the opening-mode tests alone. Instead, one should evaluate and model fracture of a textile composite under representative mixed-mode loading.

Limitations and outlook

This work focuses on monotonic tensile fracture and a specific plain-knit/soft-matrix system. Future work should address cyclic fatigue, rate dependence, and other knit topologies, and further quantify process-zone length scales and bridging statistics. Nonetheless, the present mechanism-first approach and tensile gap tests linked to a microplane-triad model exemplify a general pathway to treat fracture in soft composites with various types of textile reinforcement.

MATERIALS AND METHODS

Sample preparation and characterization

Cotton yarn (10/2 linear density) was knitted into a plain jersey architecture using a commercial weft-knitting machine (Kniterate) and embedded in PDMS (Sylgard 184, 10:1 base-to-curing-agent mass ratio). Notched specimens were cut with a flat-head blade to a consistent

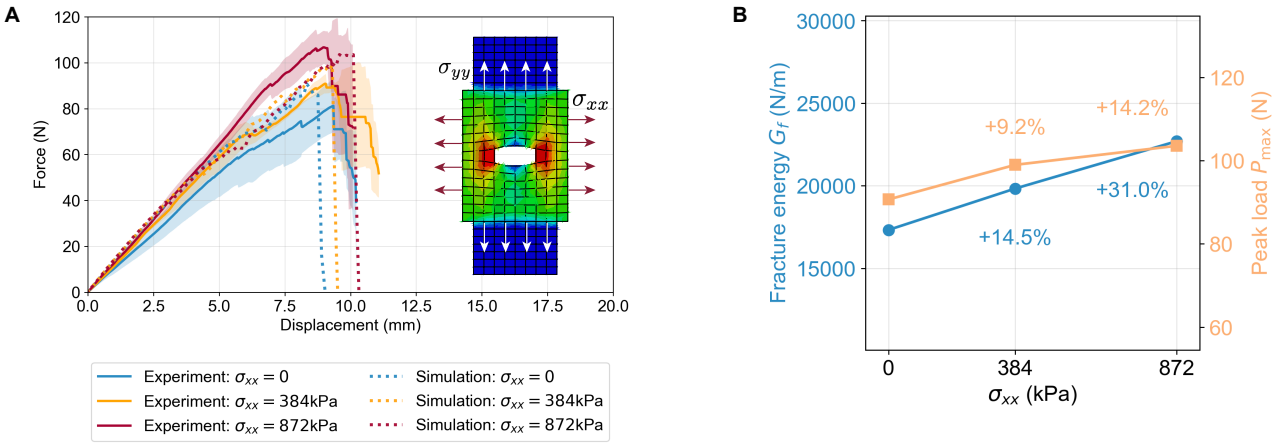

FIG. 5. Simulated responses to varying crack-parallel stresses: (A) Force–displacement curves plotted to compare with those from the experiments (plotted as the mean of at least three tests with the shaded region representing ±1 standard deviation). (B) Fracture energy G_f and peak load P_{max} as a function of the crack-parallel stress σ_{xx}.

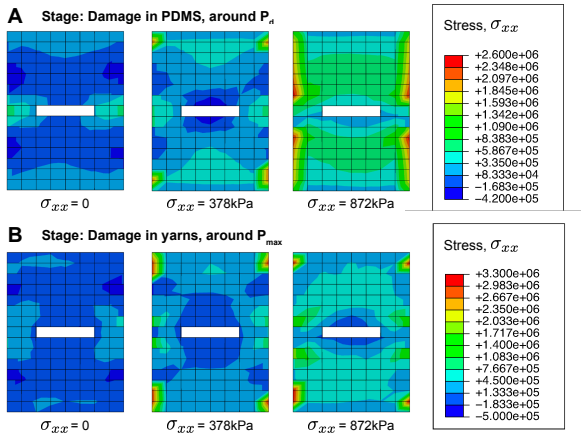

FIG. 6. Simulated field of stress σ_{xx} at critical stages during damage evolution, where shows significant crack-parallel stress effects.

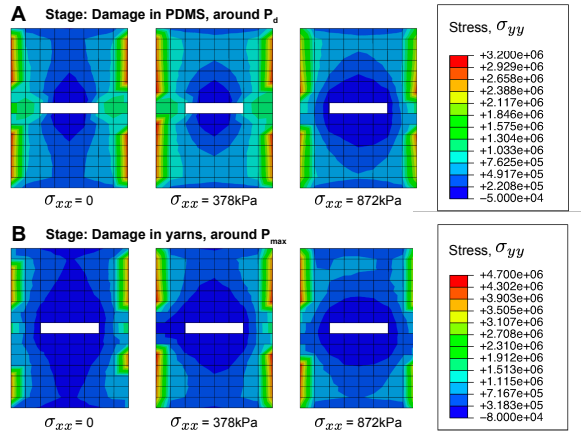

FIG. 7. Simulated field of stress σ_{yy} at critical stages during damage evolution, where shows similar crack-opening stress effects.

length, with the notch aligned along the fabric weft direction. Optical microscopy was used to measure knit spacing, notch length, RVE size, and yarn diameter for parameter calibration and defect diagnosis. Yarn and PDMS specimens fabricated under the same conditions were tested to calibrate their elastic and damage parameters, respectively; the full protocol is provided in the Supplementary Information.

Tensile gap test

Fracture tests were performed on a Fullam tester with a 100 lbf load cell under displacement control at 1 mm/min. Custom 3D-printed grippers were bonded to the specimen ends with Sil-Poxy to fit the tester, and crack propagation from the central notch was recorded using an in-situ orthogonal-projection camera. The transverse constraints imposed by the clamping clips in Fig. 1 are analogous to the gap condition originally used for stiffer materials; thus, we retain the term "gap test", although the present setup contains no physical gap.

Microplane triad model for elastic behavior

The knitted soft composite is treated as a homogenized material, whose local response is represented by an RVE, which contains a PDMS matrix and a representative plain knit stitch. Under the iso-strain assumption, both constituents experience the same macroscopic strain ε_{ij}, and the total stress is obtained by volume averaging:

$$\sigma_{ij} = \phi^{\mathrm{mat}}\sigma_{ij}^{\mathrm{mat}} + \phi^{\mathrm{yar}}\sigma_{ij}^{\mathrm{yar}}, \qquad \phi^{\mathrm{mat}} + \phi^{\mathrm{yar}} = 1, \quad (2)$$

where $\sigma_{ij}^{\mathrm{mat}}$ and $\sigma_{ij}^{\mathrm{yar}}$ are the PDMS and yarn stresses, and ϕ^{mat} and ϕ^{yar} are their volume fractions within the

RVE.

The PDMS matrix is treated as an isotropic elastic solid:

$$\sigma_{ij}^{\mathrm{mat,el}} = C_{ijkl}^{\mathrm{mat}} \varepsilon_{kl}, \tag{3}$$

where C_{ijkl}^{mat} is the isotropic stiffness tensor of the PDMS matrix.

In the present model, a continuous yarn with a realistic knitted stitch geometry [25] is represented by 16 weighted microplane triads within each RVE as shown in Fig. 2. The weights w_μ are proportional to the length of each yarn segment and normalized.

Each triad μ consists of three mutually orthogonal directions $(\mathbf{n}^\mu, \mathbf{m}^\mu, \mathbf{l}^\mu)$, where $\mathbf{n}^\mu$ is tangent to the local yarn direction, $\mathbf{m}^\mu$ lies in the transverse plane, and $\mathbf{l}^\mu$ is perpendicular to both. For clarity, unprimed indices (i, j) are used for components in the global coordinate system, whereas primed indices (i', j') are used for components in the local triad frame defined by $(\mathbf{n}^\mu, \mathbf{m}^\mu, \mathbf{l}^\mu)$. The local strain components in the triad coordinates are

$$\varepsilon_N^\mu = n_i^\mu \varepsilon_{ij} n_j^\mu, \tag{4}$$

$$\varepsilon_M^\mu = m_i^\mu \varepsilon_{ij} m_j^\mu, \tag{5}$$

$$\varepsilon_L^\mu = l_i^\mu \varepsilon_{ij} l_j^\mu, \tag{6}$$

$$\varepsilon_{MN}^\mu = \frac{1}{2}\left(n_i^\mu \varepsilon_{ij} m_j^\mu + m_i^\mu \varepsilon_{ij} n_j^\mu\right), \tag{7}$$

$$\varepsilon_{ML}^\mu = \frac{1}{2}\left(m_i^\mu \varepsilon_{ij} l_j^\mu + l_i^\mu \varepsilon_{ij} m_j^\mu\right), \tag{8}$$

$$\varepsilon_{LN}^\mu = \frac{1}{2}\left(n_i^\mu \varepsilon_{ij} l_j^\mu + l_i^\mu \varepsilon_{ij} n_j^\mu\right). \tag{9}$$

Each yarn segment is modeled as a transversely isotropic elastic solid in the local triad frame. The elastic response of the yarn is described directly by the calibrated fourth-order stiffness tensor $C_{i'j'k'l'}^{\mathrm{yar}}$, whose independent components are listed in Table I, with derivations in the Supplementary Information linking the calibrated parameters to the independent components. To represent the low initial stiffness arising from the spacing between adjacent yarn stitches before contact and locking, an additional stage is introduced through another calibrated fourth-order stiffness tensor $C_{i'j'k'l'}^{\mathrm{geo}}$. Yarn-level simulations [25] are used to identify the corresponding triads $(\mu = 2, 3, 4, 6, 7, 8, 10, 11, 12, 14, 15, 16)$, highlighted in teal color in Fig. 2C. For these triads, the components of $C_{i'j'k'l'}^{\mathrm{geo}}$ are chosen to be of the same order of magnitude as those of the matrix stiffness tensor C_{ijkl}^{mat}. The elastic stress of triad μ is then written as

$$\sigma_{i'j'}^{\mu,\mathrm{el}} = \left[(1-\alpha^\mu) C_{i'j'k'l'}^{\mathrm{geo}} + \alpha^\mu C_{i'j'k'l'}^{\mathrm{yar}}\right] \varepsilon_{k'l'}^\mu, \tag{10}$$

where the switching variable α^μ is defined by

$$\alpha^\mu = \begin{cases} 0, & \varepsilon_N^\mu < \varepsilon_{\mathrm{sw}}, \\ 1 - \dfrac{\varepsilon_{\mathrm{sw}}}{\varepsilon_N^\mu}, & \varepsilon_N^\mu \geq \varepsilon_{\mathrm{sw}}, \end{cases}$$

and $\varepsilon_{\mathrm{sw}}$ is the switching strain, calibrated from dry fabric characterization tests. For the remaining triads $(\mu = 1, 5, 9, 13)$, highlighted in red color in Fig. 2C, the calibrated yarn stiffness tensor is used directly:

$$\sigma_{i'j'}^{\mu,\mathrm{el}} = C_{i'j'k'l'}^{\mathrm{yar}} \varepsilon_{k'l'}^\mu. \tag{11}$$

Finally, the local elastic stress is transformed back to the global coordinate system and averaged over all triads:

$$\sigma_{ij}^{\mathrm{yar,el}} = \sum_{\mu=1}^{N_{\mathrm{tr}}} w_\mu \, \sigma_{ij}^{\mu,\mathrm{el}}, \qquad \sum_{\mu=1}^{N_{\mathrm{tr}}} w_\mu = 1. \tag{12}$$

Damage model

The PDMS matrix is modeled using a scalar Mazars-type damage law based on the maximum principal tensile strain. Let $\varepsilon_1 \geq \varepsilon_2 \geq \varepsilon_3$ denote the principal strains, and define the maximum positive tensile strain as

$$\varepsilon_m^+ = \langle \varepsilon_1 \rangle_+ = \max(\varepsilon_1, 0). \tag{13}$$

The damaged matrix stress is

$$\sigma_{ij}^{\mathrm{mat}} = (1 - \omega_m)\, \sigma_{ij}^{\mathrm{mat,el}}, \tag{14}$$

where ω_m is the scalar matrix damage variable. The damage evolves as

$$\omega_m = \begin{cases} 0, & \varepsilon_m^+ \leq \varepsilon_{mc}, \\ \dfrac{\varepsilon_m^+ - \varepsilon_{mc}}{\varepsilon_{mf} - \varepsilon_{mc}}, & \varepsilon_{mc} < \varepsilon_m^+ < \varepsilon_{mf}, \\ 1, & \varepsilon_m^+ \geq \varepsilon_{mf}, \end{cases} \tag{15}$$

where ε_{mc} is the onset strain for damage in the matrix and ε_{mf} is the failure strain.

The yarn damage is modeled at the microplane-triad level. For each triad μ, the yarn damage variable is

$$\omega^\mu = \max\left(\omega_N^\mu, \omega_T^\mu\right), \qquad 0 \leq \omega^\mu \leq 1, \tag{16}$$

where ω_N^μ is the axial damage driven by the local normal strain ε_N^μ, and ω_T^μ is the transverse damage driven by the equivalent transverse strain ε_T^μ defined as

$$\varepsilon_T^\mu = \sqrt{\left(\varepsilon_M^\mu\right)^2 + \left(\varepsilon_L^\mu\right)^2}. \tag{17}$$

The damaged yarn stress is

$$\sigma_{ij}^\mu = (1 - \omega^\mu)\, \sigma_{ij}^{\mu,\mathrm{el}}. \tag{18}$$

The axial yarn damage follows a two-stage law:

$$\omega_N^\mu = \begin{cases} 0, & \varepsilon_N^\mu \leq \varepsilon_{N0}, \\ (1 + R_{\mathrm{drop}})\left(1 - \dfrac{\varepsilon_{N0}}{\varepsilon_N^\mu}\right), & \varepsilon_{N0} < \varepsilon_N^\mu < \varepsilon_{N1}, \\ 1 - \dfrac{R_1}{\varepsilon_N^\mu} \exp\left[-R_2 \langle \varepsilon_N^\mu - \varepsilon_{N0} \rangle^q\right], & \varepsilon_N^\mu \geq \varepsilon_{N1}, \end{cases} \tag{19}$$

where ε_{N0} and ε_{N1} define the two-stage transition, R_{drop} controls the initial stiffness drop, and R_1, R_2, and q control the progressive softening of the remaining fibers.

The transverse yarn damage is linear:

$$\omega_T^{\mu} = \begin{cases} 0, & \varepsilon_T^{\mu} \le \varepsilon_{T0}, \\ \dfrac{\varepsilon_T^{\mu} - \varepsilon_{T0}}{\varepsilon_{Tc} - \varepsilon_{T0}}, & \varepsilon_{T0} < \varepsilon_T^{\mu} < \varepsilon_{Tc}, \\ 1, & \varepsilon_T^{\mu} \ge \varepsilon_{Tc}. \end{cases} \tag{20}$$

TABLE I. Material parameters calibrated and used in the microplane-triad simulations. The PDMS, yarn, and geometric stiffnesses are reported in terms of engineering constants

Category	Parameter	Value
Volume fraction	ϕ_m	0.72
	ϕ_y	0.28
PDMS elasticity	E_{m0}	1.51×10^6 Pa
	ν_m	0.49
PDMS damage	ε_{mc}	0.698
	ε_{mf}	0.728
Yarn material stiffness	E_N^{yar}	2.75×10^8 Pa
	E_T^{yar}	2.75×10^7 Pa
	G_{12}^{yar}	1.03125×10^7 Pa
	ν_{12}^{yar}	0.30
	ν_{23}^{yar}	0.32
Yarn geometric stiffness	E_N^{geo}	1.00×10^6 Pa
	E_T^{geo}	1.00×10^5 Pa
	G_{12}^{geo}	3.75×10^4 Pa
	ν_{12}^{geo}	0.30
	ν_{23}^{geo}	0.32
	ε_{sw}	0.12
Yarn axial damage	ε_{N0}	0.40
	ε_{N1}	0.41
	R_{drop}	9.25
	R_1	0.3076
	R_2	2.00×10^5
	q	4.25
Yarn transverse damage	ε_{T0}	0.1890
	ε_{Tc}	0.3305

For both matrix and yarn damage, the irreversibility is enforced by taking the updated damage variable as the maximum value reached in the loading history.

Finite element implementation in Abaqus

The microplane triad model is implemented as a user material subroutine (VUMAT). The simulations reproduce the boundary conditions of tensile gap tests, and the output fields are post-processed to extract: (i) the load-displacement curves, (ii) the damage zone, and (iii) the stress fields. The simulations were run in Abaqus/Explicit 2022 in double precision on an Intel Core i7-10700 CPU @ 2.90 GHz using one CPU core; excluding user-subroutine compilation and preprocessing, the wall-clock runtimes for $\sigma_{xx} = 0$, 384 kPa, and 872 kPa were approximately 20, 20, and 16s, respectively.

ACKNOWLEDGMENTS

We thank Dr. Kedar Kirane for helpful comments on the microplane triad model, Dr. Qiong Wang for helpful discussions on PDMS fabrication, and Dr. Yuming Huang for assistance with rendering the schematics in Fig. 4. We also thank Ben Zhu and Meredith Bacine for assistance with sample fabrication. H.D.E. acknowledges support from the Office of Naval Research (USA N00014-22-1-2133). J.C. acknowledges support from the Department of Defense Vannevar Bush Faculty Fellowship (USA N00014-19-1-2642).

* z-bazant@northwestern.edu
† jcao@northwestern.edu

[1] Yiyue Luo, Kui Wu, Andrew Spielberg, Michael Foshey, Daniela Rus, Tomás Palacios, and Wojciech Matusik, "Digital fabrication of pneumatic actuators with integrated sensing by machine knitting," in *Proceedings of the 2022 CHI Conference on Human Factors in Computing Systems* (2022) pp. 175:1–175:13.

[2] Vanessa Sanchez, Kausalya Mahadevan, Gabrielle Ohlson, Moritz A. Graule, Michelle C. Yuen, Clark B. Teeple, James C. Weaver, James McCann, Katia Bertoldi, and Robert J. Wood, "3D knitting for pneumatic soft robotics," Advanced Functional Materials **33**, 2212541 (2023).

[3] Mingke Wang, Yi Zhou, and Rebecca Stewart, "Soft wearable robotics: Innovative knitting-integrated approaches for pneumatic actuators design," in *Companion Publication of the 2024 ACM Designing Interactive Systems Conference* (2024) pp. 234–238.

[4] Yiyue Luo, Yunzhu Li, Pratyusha Sharma, Wan Shou, Kui Wu, Michael Foshey, Beichen Li, Tomás Palacios, Antonio Torralba, and Wojciech Matusik, "Learning human–environment interactions using conformal tactile textiles," Nature Electronics **4**, 193–201 (2021).

[5] Xiaoqian Wan, Yunchu Shen, Tian Luo, Mingming Xu, Honglian Cong, Chaoyu Chen, Gaoming Jiang, and Haijun He, "All-textile piezoelectric nanogenerator based on 3D knitted fabric electrode for wearable applications," ACS Sensors **9**, 2989–2998 (2024).

[6] Zhenghao Kou, Chao Zhang, Buyun Yu, Hao Chen, Zhenguo Liu, and Weibing Lu, "Wearable all-fabric hybrid energy harvester to simultaneously harvest radiofrequency and triboelectric energy," Advanced Science **11**, 2309050 (2024).

[7] Yi Zhou, Yilin Sun, Yangfangzheng Li, Cheng Shen, Zhiyuan Lou, Xue Min, and Rebecca Stewart, "A highly durable and UV-resistant graphene-based knitted textile sensing sleeve for human joint angle monitoring and gesture differentiation," Advanced Intelligent Systems **6**, 2400124 (2024).

[8] Ali Maziz, Alessandro Concas, Alexandre Khaldi, Jonas Stålhand, Nils-Krister Persson, and Edwin W. H. Jager, "Knitting and weaving artificial muscles," Science Advances **3**, e1600327 (2017).

[9] Jiangyu Cai, Xianrui Xie, Dandan Li, Liren Wang, Jia Jiang, Xiumei Mo, and Jinzhong Zhao, "A novel knitted

scaffold made of microfiber/nanofiber core–sheath yarns for tendon tissue engineering," Biomaterials Science **8**, 4413–4425 (2020).

[10] Xi Chen, Fengkai Liu, Yidi Lu, Zhigang Suo, and Jingda Tang, "Stretchable materials show high crack-initiation resistance that exceeds soft tissues," Materials Today **93**, 103199 (2026).

[11] Kedar Kirane, Marco Salviato, and Zdeněk P. Bažant, "Microplane-triad model for elastic and fracturing behavior of woven composites," Journal of Applied Mechanics **83**, 041006 (2016).

[12] Kedar Kirane, Marco Salviato, and Zdeněk P. Bažant, "Microplane triad model for simple and accurate prediction of orthotropic elastic constants of woven fabric composites," Journal of Composite Materials **50**, 1247–1260 (2016).

[13] Houlin Xu, Anh Tay Nguyen, and Zdeněk P. Bažant, "Sprain energy consequences for damage localization and fracture mechanics," Proceedings of the National Academy of Sciences **121**, e2410668121 (2024), https://www.pnas.org/doi/pdf/10.1073/pnas.2410668121.

[14] A. T. Nguyen, H. Xu, K. Matouš, and Z. P. Bažant, "Smooth Lagrangian crack band model based on Spress-Sprain relation and Lagrange multiplier constraint of displacement gradient," Journal of Applied Mechanics **91**, 031007 (2024).

[15] Hoang Nguyen, Madura Pathirage, Masoud Rezaei, Mohsen Issa, Gianluca Cusatis, and Zdeněk P. Bažant, "New perspective of fracture mechanics inspired by gap test with crack-parallel compression," Proceedings of the National Academy of Sciences **117**, 14015–14020 (2020).

[16] Hoang Thai Nguyen, Madura Pathirage, Gianluca Cusatis, and Zdeněk P. Bažant, "Gap test of crack-parallel stress effect on quasibrittle fracture and its consequences," Journal of Applied Mechanics **87**, 071012 (2020).

[17] Linfei Li, Boning Wang, Houlin Xu, Hoang T Nguyen, Zdeněk P Bažant, and Mija H Hubler, "Crack-parallel stress effect on fracture of fiber-reinforced concrete revealed by gap tests," Journal of Engineering Mechanics **150**, 04024011 (2024).

[18] Jeremy Brockmann and Marco Salviato, "The gap test–effects of crack parallel compression on fracture in carbon fiber composites," Composites Part A: Applied Science and Manufacturing **164**, 107252 (2023).

[19] Yang Zhao, Anh T. Nguyen, Hongshun Chen, Horacio Espinosa, and Zdeněk P. Bažant, "Crack-parallel stress effects in soft material fracture: Insights from gap tests and the microplane modeling perspective," Journal of Applied Mechanics **93**, 021001 (2025).

[20] Yu-Chuan Hsu, Zdeněk P. Bažant, and Markus J. Buehler, "Crack-parallel stress effects on fracture at the atomic scale," Journal of Applied Mechanics , 1–14 (2026), https://asmedigitalcollection.asme.org/appliedmechanics/article-pdf/doi/10.1115/1.4071779/7609595/jam-26-1080.pdf.

[21] Jian Ping Gong, Yoshinori Katsuyama, Takayuki Kurokawa, and Yoshihito Osada, "Double-network hydrogels with extremely high mechanical strength," Advanced Materials **15**, 1155–1158 (2003).

[22] Jeong-Yun Sun, Xuanhe Zhao, Widusha R. K. Illeperuma, Ovijit Chaudhuri, Kyu Hwan Oh, David J. Mooney, Joost J. Vlassak, and Zhigang Suo, "Highly stretchable and tough hydrogels," Nature **489**, 133–136 (2012).

[23] Teng Zhang, Shaoting Lin, Hyunwoo Yuk, and Xuanhe Zhao, "Predicting fracture energies and crack-tip fields of soft tough materials," Extreme Mechanics Letters **4**, 1–8 (2015).

[24] Fengkai Liu, Xi Chen, Zhigang Suo, and Jingda Tang, "Composite of knitted fabric and soft matrix. I. crack growth in the course direction," Soft Matter **20**, 9614–9621 (2024).

[25] Xiaoxiao Ding, Vanessa Sanchez, Katia Bertoldi, and Chris H. Rycroft, "Unravelling the mechanics of knitted fabrics through hierarchical geometric representation," Proceedings of the Royal Society A: Mathematical, Physical and Engineering Sciences **480**, 20230753 (2024).

[26] Krishma Singal, Michael S. Dimitriyev, Sarah E. Gonzalez, A. Patrick Cachine, Sam Quinn, and Elisabetta A. Matsumoto, "Programming mechanics in knitted materials, stitch by stitch," Nature Communications **15**, 2622 (2024).

[27] I. D. Johnston, D. K. McCluskey, C. K. L. Tan, and M. C. Tracey, "Mechanical characterization of bulk Sylgard 184 for microfluidics and microengineering," Journal of Micromechanics and Microengineering **24**, 035017 (2014).

[28] R. Moučka, M. Sedlačík, J. Osička, and V. Pata, "Mechanical properties of bulk Sylgard 184 and its extension with silicone oil," Scientific Reports **11**, 19090 (2021), article number 19090.

[29] Albert James Licup, Stefan Münster, Abhinav Sharma, Michael Sheinman, Louise M. Jawerth, Ben Fabry, David A. Weitz, and Fred C. MacKintosh, "Stress controls the mechanics of collagen networks," Proceedings of the National Academy of Sciences of the United States of America **112**, 9573–9578 (2015).

[30] Yinji Ma, Xue Feng, John A. Rogers, Yonggang Huang, and Yihui Zhang, "Design and application of "J-shaped" stress–strain behavior in stretchable electronics: a review," Lab on a Chip **17**, 1689–1704 (2017).

[31] Miklós Bergou, Max Wardetzky, Stephen Robinson, and Basile Audoly, "Discrete elastic rods," ACM Transactions on Graphics **21**, 1–12 (2008).

[32] Jonathan M. Kaldor, Doug L. James, and Steve Marschner, "Efficient yarn-based cloth with adaptive contact linearization," ACM Transactions on Graphics **29**, 1–10 (2010).

[33] A. Matzenmiller, J. Lubliner, and R. L. Taylor, "A constitutive model for anisotropic damage in fiber-composites," Mechanics of Materials **20**, 125–152 (1995).

[34] Christian Hochard, Pierre-Antoine Aubourg, and Jean-Paul Charles, "Modelling of the mechanical behaviour of woven-fabric CFRP laminates up to failure," Composites Science and Technology **61**, 221–230 (2001).

[35] Y. Thollon and C. Hochard, "A general damage model for woven fabric composite laminates up to first failure," Mechanics of Materials **41**, 820–827 (2009).

[36] S. Mukhopadhyay and S. R. Hallett, "A directed continuum damage mechanics method for modelling composite matrix cracks," Composites Science and Technology **176**, 1–8 (2019).

[37] Zdeněk P Bažant and Pere C Prat, "Microplane model for brittle-plastic material: I. theory," Journal of Engineering Mechanics **114**, 1672–1688 (1988).